Applied Surface Science 729 (2026) 166203

Contents lists available at ScienceDirect

Applied Surface Science

journal homepage: www.elsevier.com/locate/apsusc

Full Length Article

Acetic acid vapours adsorption-induced morphological change in FeBTC metal–organic framework

Davide Tocco [a], David Chelazzi [a], Andrea Salis [b,*], Emiliano Fratini [a,*], Andrea Casini [a], Rosangela Mastrangelo [a]

[a] Department of Chemistry "Ugo Schiff" & CSGI, University of Florence, via della Lastruccia 3, Sesto Fiorentino FI I-50019, Italy
[b] Department of Chemical and Geological Sciences & CSGI, University of Cagliari, SS 554 bivio Sestu, 09042 Monserrato, CA, Italy

ARTICLE INFO

Keywords:
MOFs
Volatile organic compounds
Adsorption
Morphology
Acetic Acid
FeBTC

ABSTRACT

We report a post-synthetic vapour phase modulation strategy to tailor the morphology of semicrystalline FeBTC metal–organic frameworks (MOFs) via acetic acid (AcOH) vapours adsorption. FeBTC, synthesized through a green one-pot route, retained its structure upon exposure to AcOH vapours, as confirmed by WAXS. Adsorption kinetics followed a double-exponential model, reaching 0.87 ± 0.09 mg·mg^{-1} uptake at 237 h. μFTIR spectroscopy demonstrated a uniform distribution of AcOH on FeBTC surface, whereas thermogravimetric analysis (TGA) provided insights into the thermal stability and AcOH desorption behaviour of FeBTC, supporting the evidence of AcOH interaction with the MOF. Scanning electron microscopy (SEM) revealed rapid transformation from irregular, blocky particles to hollow, cylinder-like architectures within 14 h upon interaction with AcOH vapours. This morphological change was confirmed by USAXS/SAXS data, which also showed a steep relative increase in surface/volume (S/V) ratio at early exposure followed by a decrease at later stages compared to the initial value. This facile vapour phase modulator approach unlocks new possibilities for post-synthetic control of MOF morphology and available interaction surface, with implications for gas capture, catalysis, and separation.

1. Introduction

Metal–organic frameworks (MOFs) are three-dimensional networks composed of metal ions and organic linkers [1–3], which are emerging as promising materials for gas adsorption [4], catalysis [5,6], supports for enzyme immobilisation [7–11], removal of water pollutants [12], and volatile organic compounds (VOCs) capture [13]. According to the United States Environmental Protection Agency, 50% of VOCs emissions result from fossil fuel combustion [14]. However, VOCs also come from the degradation of various materials, e.g., cellulose-based materials or poly(vinyl acetate) adhesives/coatings that lead to the formation of acetic acid (AcOH) [15]. Notably, in addition to health hazards, AcOH is also one of the primary VOCs found in museums and collections [16], where it represents a drastic issue for the integrity of manuscripts, documents, and artworks. The development of materials able to capture AcOH thus plays a crucial role for health/environment and even cultural heritage preservation. Dedecker et al. [17] recently showed that UiO-66 MOF, modified with hydrophobic –CF_3 groups, exhibited improved AcOH adsorption at low pressures compared to other MOFs. Mohtar et al. [18] reported the application of MIL-100 (Fe) as an adsorbent for AcOH in the preservation of cellulose acetate-based cinematographic and photographic films [18]. Recently, Severino et al. reported on MOFs composed of trinuclear [M_3(μ3-O)] (M = Fe^{3+}, Cr^{3+}, Al^{3+}) clusters, such as MIL-100 (Fe), enabling the selective capture of polar VOCs such as AcOH, even in the presence of water. This was due to the presence of coordinatively unsaturated (open) metal Fe^{3+} sites of [Fe_3(μ3-O)] obtained by removing terminal –H_2O ligands at 150 °C [13]. Nevertheless, these approaches are still scarcely sustainable, being limited by either high costs or time-consuming synthetic pathways that use high temperatures or organic solvents (i.e. DMF), with a poor environmental profile [18]. These concerns can be addressed through the use of semicrystalline MOFs, which are typically obtained in short time under mild reaction conditions. However, the current gap to this approach concerns the unknown effects caused by vapour-phase AcOH adsorption on the semicrystalline MOF structure, which is the objective and novelty of this contribution. In particular, FeBTC MOF (the semicrystalline counterpart of MIL-100 (Fe)) [19,20], can be synthesized via a fast and green one-pot synthesis [19,21,22]. Due to the presence of open metal sites generated

* Corresponding authors.
E-mail addresses: asalis@unica.it (A. Salis), emiliano.fratini@unifi.it (E. Fratini).

https://doi.org/10.1016/j.apsusc.2026.166203
Received 26 November 2025; Received in revised form 31 January 2026; Accepted 3 February 2026
Available online 3 February 2026

by thermal activation [20], FeBTC may promote the selective adsorption of carboxylic acids over water [20]. However, while the use of AcOH as a modulator to control MOF pore size, structure, and morphology during the synthesis is well documented in the literature [23,24], to the best of our knowledge, the effect of AcOH vapours on post-synthesized semi-crystalline MOFs has not been investigated yet. The carboxylic groups of modulators form clusters with metal cations, thereby influencing the crystallization processes during MOF formation [25]. However, it remains unclear if similar interactions can occur between AcOH vapours and metal centres in already-formed frameworks, potentially altering their structure or morphology after the synthesis.

Here, we used FeBTC as an AcOH adsorbent (Scheme 1, Fig. S1 in Supplementary Material), looking into the physico-chemical transformations induced by AcOH vapours in the MOF structure and morphology. The FeBTC pre- and post-AcOH exposure was characterised through wide, small, and ultra-small angle X-ray scattering (WAXS, SAXS, USAXS), scanning electron microscopy (SEM), Raman spectroscopy, FTIR spectroscopy and imaging, as well as thermogravimetric analysis (TGA) aiming to understand chemical, structural and morphological changes.

2. Materials and methods

2.1. Chemicals

Sodium hydroxide (NaOH), 1,3,5-benzenetricarboxylic acid (H_3BTC, ≥95%) and acetic acid (AcOH, ≥99%) were purchased from Sigma-Aldrich. Iron(III) acetate was synthesized and purified in-house. All reagents were used as received without further purification. Milli-Q water (≥ 18.2 MΩ cm) was used to prepare all aqueous solutions.

2.2. Synthesis of FeBTC MOF

FeBTC MOF was synthetized according to Sanchez-Sanchez et al. [22]. Briefly, 1,3,5-benzenetricarboxylic acid (H_3BTC, 0.263 g) was dissolved in NaOH (3.685 mL, 1.06 M) and H_2O (6.388 mL). $FeCl_3{\cdot}6H_2O$ (0.508 g) was dissolved in H_2O (10 mL) and added dropwise to the H_3BTC solution under stirring at 25 °C for 10 min. The resulting precipitate was collected by filtration, washed several times with Milli-Q water, and dried at room temperature.

2.3. Adsorption kinetics of AcOH vapours on FeBTC MOF

Adsorption tests under saturated AcOH atmosphere were performed using a modified 250 mL Erlenmeyer flask with a small inner cup (2 mL), as schematically illustrated in Fig. S1 (Supplementary Material), containing 15 mg of activated FeBTC sample. The process of activation was carried out by thermal treatment in an oven at 393 K under vacuum for several hours (>3 h). After activation, the material was cooled down to 296 K in a desiccator. Subsequently, an amount of FeBTC was placed in the modified 250 mL Erlenmeyer flask, and then 2 mL of glacial AcOH was added to the bottom of the flask, surrounding the cup. Subsequently, the system was sealed to allow the AcOH vapours to saturate the flask and to be adsorbed onto the FeBTC samples over various exposure times up to about 10 days (i.e., 237 h). Afterward, the FeBTC samples were removed and immediately weighed. The results were expressed as milligrams of adsorbed AcOH per milligram of FeBTC, plotted versus exposure time. Each adsorption experiment was repeated at least three times.

2.4. Characterization of FeBTC

Samples' morphology was characterized by electron microscopy using a Field Emission Gun Scanning Electron Microscope SIGMA (FEG-SEM, Carl Zeiss Microscopy GmbH, Germany), with an acceleration potential of 5 kV and a working distance of about 5–6 mm. Prior to SEM analysis, dried samples were covered with gold by an Agar Scientific Auto Sputter Coater. IR analysis of sample powders was carried out via μFTIR and ATR-FTIR without any pre-treatment. μFTIR was carried out with a Cary 670 FTIR spectrophotometer coupled to a Cary 620 FTIR microscope (Agilent Technologies), using a 15× Cassegrain objective. Measurements were carried out in reflectance mode over the powders, while background spectra were collected on a gold-plated surface. The experimental conditions were: spectral range of 3900–900 cm^{-1}, 512 scans for each acquisition, spectral resolution of 2 cm^{-1}, open windows. A 128 × 128 pixels Focal Plane Array (FPA) detector was used for the 2D μ-FTIR Imaging; the pixel size is 5.5 μm × 5.5 $μm^2$, and each pixel provides an independent spectrum from the sample's surface. Each analysis delivers the spectra of a 700 × 700 $μm^2$ "tile" with 16,384 independent spectra. ATR-FTIR was carried out with a Thermo Nicolet Nexus 870 spectrometer, using a single reflection diamond crystal ATR unit, a spectral range of 4000–650 cm^{-1}, 128 scans and a spectral resolution of 2 cm^{-1}. An inVia Qontor confocal microRaman (Renishaw) was used to acquire Raman spectra. The instrument is equipped with a solid-state laser (785 nm, IPS R-type NIR785, 200 mW, 1200 l/mm grating), a front-illuminated CCD camera (655 × 1024 px) and a research-grade Leica DM 2700 microscope. TGA was carried out by a Discovery SDT 650 (TA Instruments) in a temperature range from 25 to 700 °C and a heating ramp of 10 °C min^{-1}, under continuous N_2 flow (flow rate = 40 mL min^{-1}). USAXS/SAXS/WAXS measurements were performed on a Xeuss 3.0 HR (Xenocs, Grenoble, France) equipped with an EIGER2R (1 M model) hybrid pixel photon counting detector (Dectris Ltd., Baden, Switzerland) consisting of 1028 × 1062 pixels with a size of 75 × 75 $μm^2$. The wavelength of the X-ray beam was λ = 1.542 Å. Calibration of the sample to detector distance was performed using silver behenate (d = 58.38 Å). Three sample-to-detector distances, 60, 450 and 1800 mm, were used to access a range of scattering vectors, Q, going from 0.005 to 2.77 $Å^{-1}$, with Q=(4π/λ)sinθ and 2θ the scattering angle,

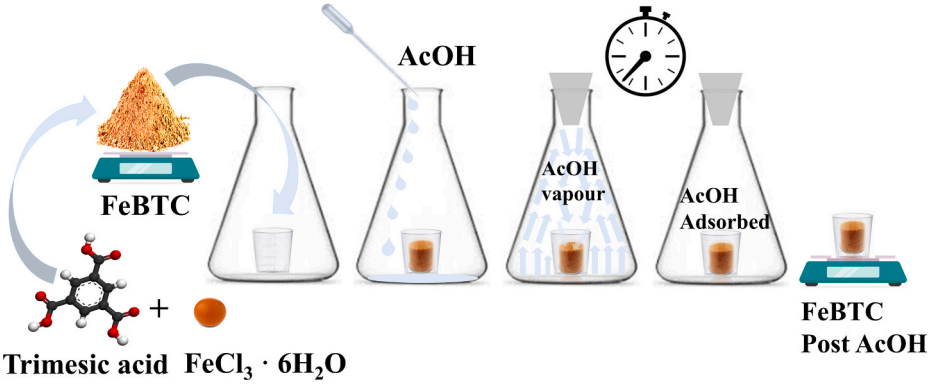

Scheme 1. Preparation of FeBTC and AcOH adsorption.

thus covering the SAXS/WAXS regions. USAXS measurements were performed with the Bonse-Hart configuration, covering the 0.0002–0.01 $Å^{-1}$ range. Powders were enclosed in sealed demountable cells using Kapton® foils as windows. The 1D azimuthally averaged scattering patterns were reduced by subtracting the scattering intensity from empty holder (SAXS and WAXS) and by merging the curves obtained at the two largest sample-to-detector distances for SAXS. Data reduction, normalization, and merging was performed in XSACT (X-ray Scattering Analysis and Calculation Tool, Xenocs, France). SAXS data analysis was performed through SASView Software [https://www.sasview.org/], according to the mathematical model reported in Supplementary Material. USAXS data were desmeared (centering method: center of mass), while their high-Q extrapolation was performed by using a fractal model. Slope values in the 0.0002–0.002 $Å^{-1}$ range were analyzed.

3. Results and discussion

The WAXS patterns, reported in Fig. 1A, show peaks at 11°, 19°, 24° and 28°, confirming the formation of FeBTC structure [8,12]. The FeBTC pattern is not well defined due to the semi-crystalline nature of the material [26]. The adsorption kinetics of AcOH on FeBTC was investigated by weighing the MOF sample at different times of exposure in an atmosphere saturated with AcOH vapours at 23 °C. The adsorption kinetic curve, reported in Fig. 1B, showed a maximum AcOH uptake of 0.87 ± 0.09 mg per mg of FeBTC at 237 h. This value is higher than that reported by Cruz et al., who obtained an AcOH adsorption of 0.48 $mg{\cdot}mg^{-1}$ under identical experimental conditions, namely exposure to glacial acetic acid saturated vapour (partial pressure ≈ 2.0 kPa at 296 K), the same temperature range, and a comparable exposure protocol [27]. Recently, Zuliani et al. developed a ZnO-based system for AcOH capture, reporting an uptake of 0.85–1.15 $mg{\cdot}mg^{-1}$; however, in that system the reported adsorption capacity was reached only after prolonged exposure times (approximately 1600 h), indicating significantly slower adsorption kinetics compared to FeBTC under analogous vapour-phase conditions [28]. This points to the high adsorption capability of the MOF. Experimental adsorption data were fitted with the pseudo–first–order and pseudo–second–order models (Supplementary Material, Fig. S2) and with a double–exponential model (Fig. 1B). Among these, the latter function afforded the best agreement with the data (Fig. 1B), revealing two kinetically distinct uptake regimes [29] likely ascribable to AcOH physisorption and chemisorption onto FeBTC, respectively [28,30]. While the double-exponential model captures the presence of a fast and a slow contribution, it is an empirical descriptor and, by itself, does not determine the chemical nature of the underlying steps. Therefore, the mechanistic assignment is established from independent thermo–spectroscopic measurements discussed below.

The WAXS pattern obtained for FeBTC exposed to AcOH vapours for 237 h (Fig. 1A) is similar to that of FeBTC before AcOH exposure, demonstrating that AcOH does not alter the MOF structure, as also observed by Serre et al. [17]. Thermogravimetric profiles of FeBTC samples exposed to AcOH vapours for different times (0 h, 24 h, 48 h, 120 h, and 237 h), shown in Fig. 1C and listed in Table S1, display multistep thermal decompositions. The pristine FeBTC sample exhibited a mass loss of 6.7%wt in the 30–130 °C range, attributed to the desorption of adsorbed water. Higher mass losses of 14.5%wt and 22.9% wt were observed in the 130–417 °C and 417–534 °C ranges, respectively, due to the breakdown of the FeBTC framework. A further mass loss of 11.5%wt occurred above 570 °C and could be associated with carbonisation processes [31]. Upon exposure to AcOH vapours, the thermogravimetric profiles changed significantly. After 24 h and 48 h of AcOH vapours exposure, FeBTC exhibited higher mass losses of 11.4%wt and 14.9%wt, respectively, within the 30–110 °C range compared to the pristine material, likely due to the desorption of both water and acetic acid. The 48 h sample exhibited more distinct thermal transitions, with mass losses (8.6%wt, 6.9%wt, and 9.4%wt) in the 110–417 °C range. Notably, after 120 h the sample showed a broadened mass loss event, with a 17.0%wt loss extending up to 210 °C, suggesting stronger guest-framework interactions or deeper incorporation of AcOH. This interpretation is further supported by the TGA of iron(III) acetate, whose decomposition occurs over a comparable temperature window (Supplementary Material, Fig. S5F), consistent with the formation of Fe–acetate–like coordinated species in the chemisorbed fraction.

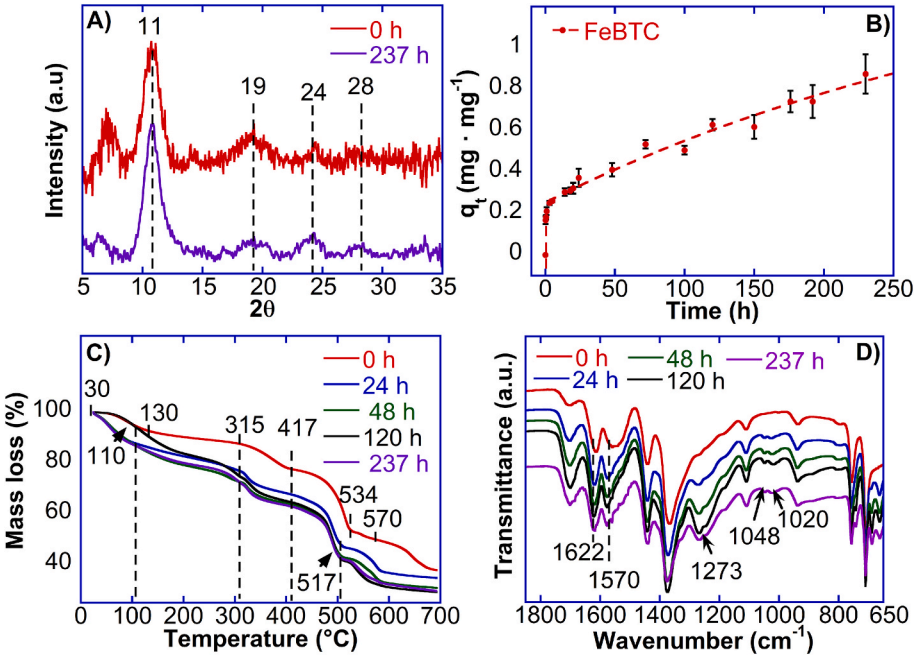

Fig. 1. **(A)** WAXS patterns of FeBTC pre- and post- AcOH adsorption. **(B)** Adsorption of AcOH by FeBTC sample in saturated atmosphere of AcOH at 23 °C (fit to a double-exponential adsorption kinetic model). **(C)** Thermogravimetric profiles from 30 °C to 700 °C under N_2 of FeBTC and FeBTC exposed to AcOH vapours for different times (0 h, 24 h, 48 h, 120 h, and 237 h). **(D)** ATR FT-IR spectrum wavenumber ranges from 450 to 2000 cm^{-1} of FeBTC and FeBTC exposed to AcOH vapours for different times (0 h, 24 h, 48 h, 120 h, and 237 h).

Moreover, the overall high–temperature behaviour is fully consistent with the involvement of chemisorbed AcOH species, as also supported by the high–temperature DTG peaks and their evolution with exposure time observed in Fig. S5 (Supplementary Material). In contrast, the sample at 237 h showed a reduced mass loss of 8.6%wt in the 30–110 °C range, indicating a lower amount of physisorbed species. The 120 h and 237 h samples decomposed via similarly resolved multi-step patterns between 215 and 517 °C. All AcOH exposed samples showed a final mass loss of 10–12%wt above 570 °C ascribable to carbonaceous residue formation.

ATR-FTIR spectra of FeBTC pre and post AcOH capture are shown in Fig. 1D. Due to AcOH vapours exposure, FeBTC showed new peaks at 663 cm^{-1} and 689 cm^{-1}, 1020 cm^{-1} and 1048 cm^{-1}. Moreover, the C=O stretching of carboxylate groups shifted from 1615 cm^{-1} to 1622 cm^{-1}, [32] whilst the symmetric stretching bands of the O–C–O group at 1365 cm^{-1} shifted to 1376 cm^{-1},[4,33,34] likely due to AcOH adsorption. These spectral changes are consistent with stronger host–guest interactions, supporting the involvement of chemisorbed AcOH species.

FTIR 2D imaging provided further insight into the spatial distribution of adsorbed AcOH within the FeBTC sample (Fig. 2A–E). Mapping the absorbance intensity (peak area) in the 1010–1060 cm^{-1} region, corresponding to the C–O stretching vibration of AcOH, revealed that the molecule is distributed throughout the entire MOF structure in alternating domains and gaps of 10–100 μm (detection limit is of ca. 0.02 pg/μm^2) [35].

Fig. 3 shows the SEM micrographs of FeBTC samples before AcOH exposure and at different adsorption times in the range 0–237 h (see further cases in Fig. S6). Over the range of 0 and 5 h the FeBTC exhibited its characteristic rough, irregular, blocky structure. Surprisingly, after 14 h of exposure to AcOH, the material morphology re-arranged, changing from irregular structures to hollow, cylinder-like objects.

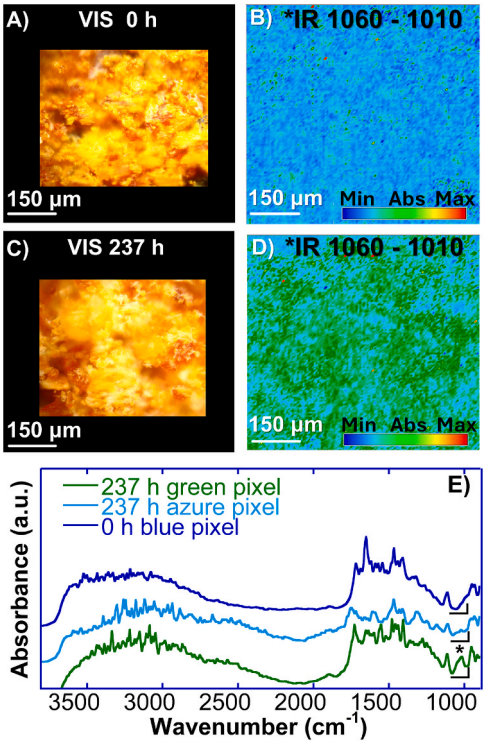

Fig. 2. (A,B) Visible and **(C,D)** FTIR 2D Imaging maps of the pristine FeBTC and FeBTC exposed to AcOH (237 h), respectively. IR map detail of micrometric domains of concentrated AcOH (Green pixels). **(E)** Reflectance spectra of pristine FeBTC and FeBTC post AcOH. The spectra of FeBTC are related to green, azure and blue pixels (5.5 × 5.5 μm^2 each) of the IR maps. The "*" and brackets highlight the C–O stretching vibration of AcOH (1060–1010 cm^{-1}) and the spectral region that was imaged in the maps.

After 48 h of exposure to AcOH, the FeBTC surface was fully covered by these structures. This indicates a significant interaction between AcOH and the FeBTC material. Changes in the MOF morphology upon exposure to acetic acid were investigated at different lengthscales, along with the variation in surface area, through scattering measurements. Compared to other techniques (i.e. N_2 adsorption/desorption isotherms), SAXS has the advantage of not requiring pre-treatment steps that may alter the samples. Fig. S7 (Supplementary Material) shows the SAXS profiles of the pristine sample and the samples exposed to the saturated AcOH atmosphere (0.25–237 h), acquired in the 0.005–0.1 $Å^{-1}$ range. The change in the Surface/Volume (S/V) ratio was calculated according to the method described by Spalla *et al.* [36] In detail, the $I \times Q^4$ values registered in the high-Q region of the Porod plot (see dotted lines in Fig. 4A) were used to calculate the relative surface area variation (%) with respect to the pristine sample, as described in the Materials and Methods section. The data, plotted in Fig. 4B, show that S/V increased up to 15 times ca. its initial value after 0.25 h, and later decreased, finally stabilizing at values comparable to the pristine sample at 237 h. The samples' morphological evolution at the micro-, submicro- and nano-scale was investigated through USAXS and SAXS, accessing inhomogeneities in the 3 μm–1 nm range.

Representative samples to be analyzed were selected from the SEM images. SAXS data (Fig. 4C) are characterized by a Porod's slope at low-Q and pronounced bumps, occurring at Q_1, ~2 × Q_1, ~3 × Q_1, being Q_1 = 0.14 $Å^{-1}$ (see Supplementary Material, fitting eq. S10 and Table S2). This value can be linked to layered spheres, with a radius $r \sim 4.5$ nm, suggesting that the microscale cylinders are indeed aggregates of nanoparticles. Indeed, the presence of spherical nanoparticles that rearrange upon AcOH adsorption is confirmed by SEM imaging (Fig. 3 and S6, right panels). Nonetheless, high-Q bumps may also indicate a locally ordered pore arrangement, as reported for other MOFs [20,37,38]. The bumps, fitted according to Gaussian peaks, increase in intensity over time, up to 120 h. The pristine sample (0 h) does not follow this trend, due to an excess background scattering, linked to inhomogeneities smaller than 10 nm (visible at $Q > 0.06$ $Å^{-1}$). The latter can be due to the MOF mesopores. The Porod's slopes, *n*, describing the low-Q SAXS data are listed in Table 1. *n* values indicate an almost smooth surface [39], linked to objects larger than ~100 nm. Larger lengthscales were probed through USAXS measurements. In the USAXS range, the samples' fractality exhibits two different regimes, described by two slopes in the low-Q (0.0002–0.0003 $Å^{-1}$, ~3.4–2.3 μm) and high-Q regions (0.0003–0.001 $Å^{-1}$, ~2.3–0.6 μm), both listed in Table 1. Indicative values are reported for the low-Q slopes, due to the limited number of experimental points available in the 0.0002–0.0003 $Å^{-1}$ range. The low-Q slopes decreased with exposure times higher than 48 h: values smaller than 3 indicate less dense objects, forming at later stages of the adsorption process. This is an indication of the structure rearrangement from bulk-like material to a more open structure composed by hollow cylinders with pores in the sub-micron scale, in agreement with the details observed in SEM images (Fig. S6, Supplementary Material file). USAXS high-Q slopes are generally the same as the Porod exponents obtained in the SAXS region. Therefore, similarly to SAXS Porod slopes, also USAXS high-Q slopes indicate smooth surfaces, but in the 2 μm – submicron region. Similar slopes have been observed in other MOFs [38,40].

The drastic morphological rearrangement of FeBTC upon exposure to AcOH vapours has not been previously discussed in the literature and deserves to be discussed in further detail. Since condensation of AcOH within the MOF pores is expected according to the Kelvin equation, condensed AcOH may coordinate to open Fe metal sites, as previously described by Severino et al. [13]. As a matter of fact, liquid AcOH is known to be a common modulator in specific MOF synthesis [23]. In this case, the open Fe sites are expected to bind the AcOH's C=O group, leading to the formation of a modified complex. The Fe-acetate complexes are generally known to be amorphous, with an elongated morphology at the microscale [41,42]. The TGA profile of analogous

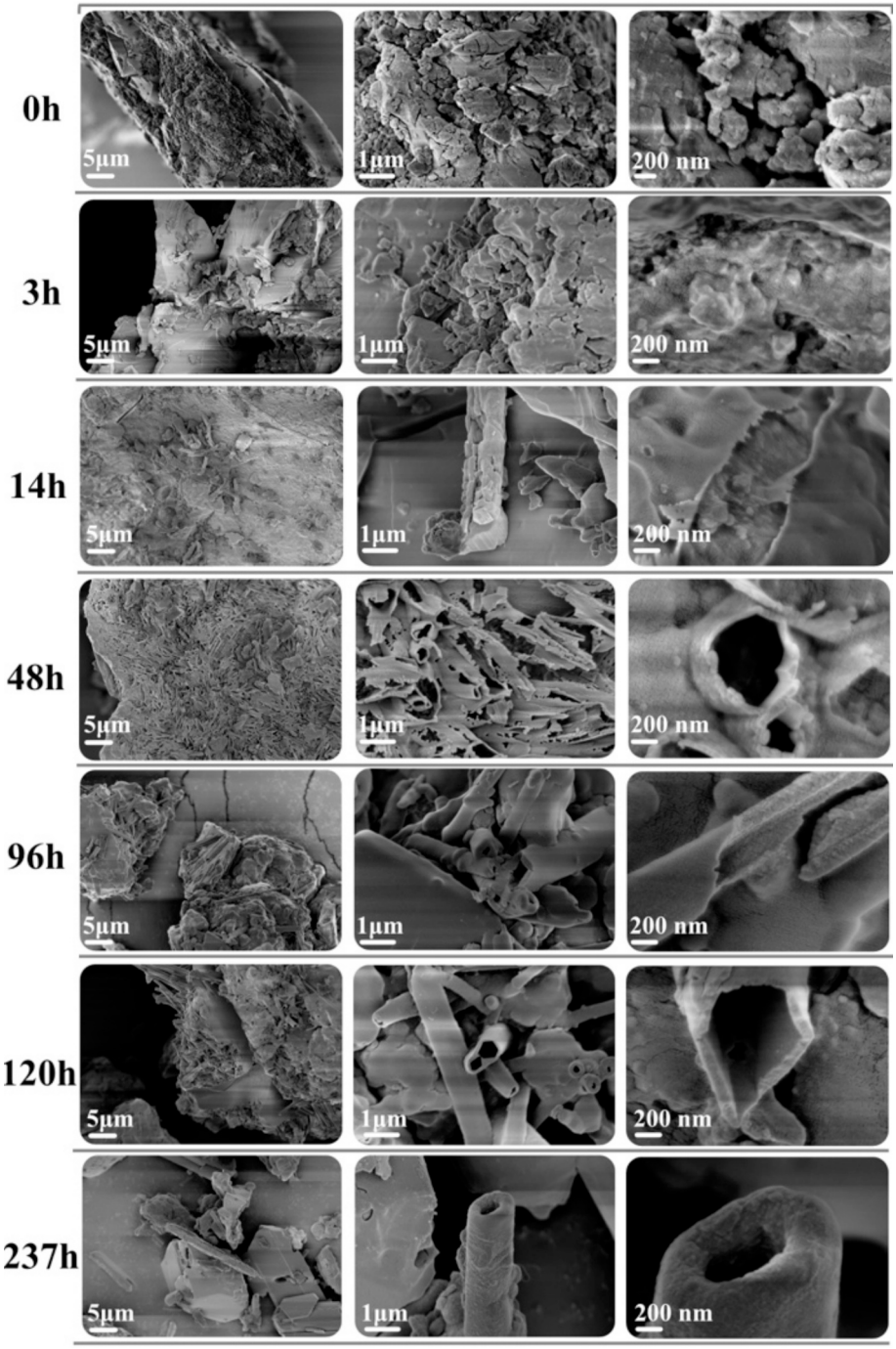

Fig. 3. SEM images of FeBTC exposed to AcOH over a time range from 0 to 237 h.

complexes shows weight losses comparable to those of the AcOH-exposed FeBTC reported in the current work (Fig. S5F). As for the current study, AcOH vapours might contribute to lowering the energy of activation and accelerating the recombination of coordination bonds between metal ions and carboxylate ligands, similarly to the case reported by Sakata et al. [43] In other words, in this case AcOH serves both as a linker for the exposed Fe sites and as a trigger for the rupture and recombination of coordination bonds between iron nodes and organic ligands, resulting in a structural rearrangement and the formation of the MOF's elongated morphology (see Fig. S6).

4. Conclusions

In summary, we investigated semicrystalline FeBTC as an AcOH adsorbent prepared via a rapid one-pot route. Time-resolved uptake measurements yielded adsorption kinetics best described by a double-exponential model, indicating two kinetic steps, while TGA, and FTIR analyses on pre- and post-adsorption samples confirmed effective AcOH uptake. Importantly, because the double-exponential function is empirical and does not by itself resolve the nature of the elementary steps, we relied on thermo-spectroscopic evidence to assign the underlying mechanism. TGA shows that the progressive increase in low-temperature mass loss ($\leq$110–130 °C) upon AcOH exposure, from 6.7 %wt in pristine FeBTC to 11.4 %wt and 14.9 %wt after 24 h and 48 h, is

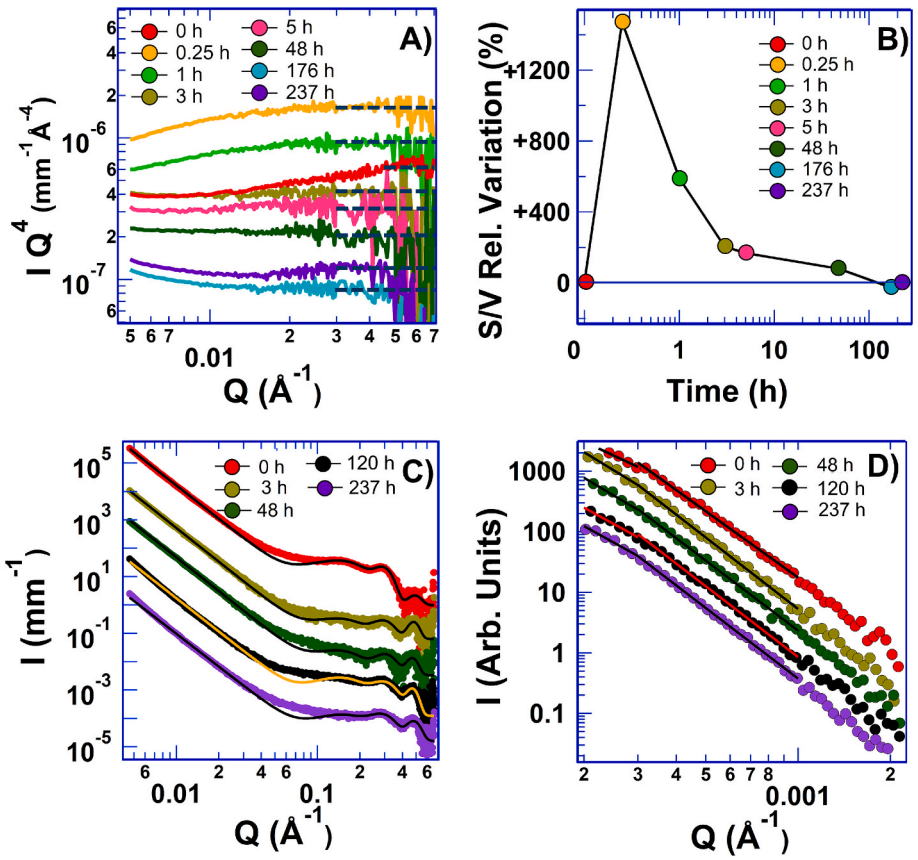

Fig. 4. **(A)** Porod's plot of the data shown in Fig. S7; **(B)** Variation of the Surface/Volume ratio upon exposure (point "0h" location is a guide to the eye); **(C)** SAXS profiles in the 0.005–0.66 $Å^{-1}$ range (markers) and fitting (lines) of selected samples; **(D)** USAXS profiles in the 0.0002–0.003 $Å^{-1}$ range of selected samples.

Table 1
SAXS and USAXS fitting parameters of the 0 h–237 h samples: Porod scale factor A, Porod exponent *n*, and USAXS slopes at low- and high-Q.

SAXS USAXS				
Time (h)	A (Scale), x 10^{-7}	n (Porod, low-Q)	Low-Q Slope	High-Q Slope
0	6.61 ± 0.05	3.90 ± 0.05	−2.4*	−3.6 ± 0.1
3	1.03 ± 0.05	3.95 ± 0.05	−3.1*	−3.9 ± 0.1
48	1.80 ± 0.05	3.95 ± 0.05	−3.0*	−3.9 ± 0.1
120	2.20 ± 0.05	3.90 ± 0.05	−2.8*	−3.9 ± 0.1
237	1.80 ± 0.05	3.85 ± 0.05	−2.8*	−3.9 ± 0.1

*Apparent value, due to the limited number of experimental points available.

attributable to desorption of physisorbed species, whereas new, well-defined weight-loss events between 110 and 417 °C appearing after 48 h, together with DTG peaks centred at ~290–300 °C that intensify with exposure time, reveal a more strongly bound fraction. These thermal signatures closely resemble those of iron(III) acetate, supporting the formation of Fe-acetate-like coordinated complexes. Consistently, ATR-FTIR (Fig. 1D) exhibits AcOH-related bands (1020–1048 cm^{-1}) and shifts in the C=O and O–C–O regions (1615 → 1622 cm^{-1}; 1365 → 1376 cm^{-1}), compatible with coordination to open Fe^{3+} Lewis-acid sites. Altogether, the data indicate that AcOH adsorption on FeBTC proceeds via an initial rapid physisorption step followed by slower chemisorption involving coordinated AcOH species, in full agreement with the two-step kinetics captured by the double-exponential model. Unexpectedly, AcOH vapour exposure also triggers a striking morphological transformation without detectable changes in the WAXS pattern: the specific surface-to-volume ratio increases sharply at early exposure (up to ~15 × the initial S/V) and the material evolves from irregular grains to hollow, cylinder-like architectures, as shown by SEM and SAXS/USAXS. While AcOH is well known as a solution-phase synthesis modulator [44], its post-synthetic vapour-phase action on semicrystalline MOFs has, to our knowledge, not been reported before. Given the pivotal role of morphology and accessible surface in MOF performance (e.g., catalysis, gas storage and separations) [45], the ability to tailor these properties post-synthesis via mild vapour-phase modulators such as acetic acid may open new opportunities across MOF applications.

CRediT authorship contribution statement

Davide Tocco: Writing – review & editing, Writing – original draft, Visualization, Methodology, Investigation, Formal analysis, Data curation, Conceptualization. **David Chelazzi:** Writing – review & editing, Validation, Investigation, Funding acquisition. **Andrea Salis:** Writing – review & editing, Writing – original draft, Validation, Methodology, Investigation, Formal analysis, Conceptualization. **Emiliano Fratini:** Supervision, Funding acquisition, Conceptualization. **Andrea Casini:** Writing – review & editing, Investigation. **Rosangela Mastrangelo:** Writing – review & editing, Writing – original draft, Methodology, Investigation, Data curation.

Declaration of competing interest

The authors declare that they have no known competing financial interests or personal relationships that could have appeared to influence the work reported in this paper.

Acknowledgements and funding sources

CSGI and the European Union (GREENART project, Horizon Europe research and innovation program under grant agreement no. 101060941) are gratefully acknowledged for partial financial support. Views and opinions expressed are, however, those of the author(s) only and do not necessarily reflect those of the European Union or the European Research Executive Agency (REA). Neither the European Union nor the granting authority can be held responsible for them.

The financial support provided by the MUR - Dipartimenti di Eccellenza 2023–2027 (DICUS 2.0) to the Department of Chemistry "Ugo Schiff" of the University of Florence is also acknowledged. DT acknowledges financial support by the Regione Toscana (FSC 2014–2020, GiovaniSi acronim project QD4PH, CUP: B13D21008630008). AS thanks FIR 2024 for funding. The authors are grateful to Dr. Fabio Manna (University of Cagliari, Italy) for providing a sample of the iron(III) acetate. Dr. Cristina Carucci (University of Cagliari, Italy) is acknowledged for carrying out the TG analysis of iron (III) acetate.

Appendix A. Supplementary data

The following files are available free of charge. Further details on materials and methods; fitting equations; further SEM images; further comments on SAXS fitting results; Raman spectra of FeBTC and FeBTC exposed to AcOH vapours for different times (0 h, 24 h, 48 h, 120 h, and 237 h); thermogravimetric profiles from 30 °C to 700 °C under N_2 of FeBTC and FeBTC exposed to AcOH vapours for different times (0 h, 24 h, 48 h, 120 h, and 237 h). Supplementary data to this article can be found online at https://doi.org/10.1016/j.apsusc.2026.166203.

Data availability

The data supporting this article have been included as part of the Supplementary Material file. Further data will be made available on request.

References

[1] R. Robson, A net-based approach to coordination polymers, J. Chem. Soc. Dalt. Trans. (2000) 3735–3744, https://doi.org/10.1039/b003591m.
[2] S.R. Batten, N.R. Champness, X.-M. Chen, J. Garcia-Martinez, S. Kitagawa, L. Öhrström, M. O'Keeffe, M. Paik Suh, J. Reedijk, Terminology of metal–organic frameworks and coordination polymers (IUPAC recommendations, Pure Appl. Chem. 85 (2013) (2013) 1715–1724, https://doi.org/10.1351/PAC-REC-12-11-20.
[3] H. Furukawa, K.E. Cordova, M. O'Keeffe, O.M. Yaghi, The Chemistry and Applications of Metal-Organic Frameworks, Science (80-.). 341 (2013) 1230444. doi:10.1126/science.1230444.
[4] G. Autie-Castro, M.A. Autie, E. Rodríguez-Castellón, C. Aguirre, E. Reguera, Cu-BTC and Fe-BTC metal-organic frameworks: role of the materials structural features on their performance for volatile hydrocarbons separation, Colloid. Surf. A Physicochem. Eng. Asp. 481 (2015) 351–357, https://doi.org/10.1016/j.colsurfa.2015.05.044.
[5] K. Hemmer, M. Cokoja, R.A. Fischer, Exploitation of intrinsic confinement effects of MOFs in catalysis, ChemCatChem 13 (2021) 1683–1691, https://doi.org/10.1002/cctc.202001606.
[6] A. Belcovici, D. Tocco, E. Fratini, A. Salis, G.L. Turdean, Composite material based on ZIF-8, reduced graphene oxide, and Nafion as electrode modifier for dopamine electrooxidation, Microchem. J. 216 (2025) 114769, https://doi.org/10.1016/j.microc.2025.114769.
[7] D. Tocco, D. Chelazzi, R. Mastrangelo, A. Casini, A. Salis, E. Fratini, P. Baglioni, Conformational changes and location of BSA upon immobilization on zeolitic imidazolate frameworks, J. Colloid Interf. Sci. 641 (2023) 685–694, https://doi.org/10.1016/j.jcis.2023.03.107.
[8] D. Tocco, C. Carucci, D. Todde, K. Shortall, F. Otero, E. Sanjust, E. Magner, A. Salis, Enzyme immobilization on metal organic frameworks: Laccase from Aspergillus sp. is better adapted to ZIF-zni rather than Fe-BTC, Colloid. Surf. B Biointerf. 208 (2021) 112147, https://doi.org/10.1016/j.colsurfb.2021.112147.
[9] D. Tocco, M. Joshi, R. Mastrangelo, E. Fratini, A. Salis, M. Hartmann, A green approach to encapsulate proteins and enzymes within crystalline lanthanide-based Tb and Gd MOFs, Dalt. Trans. 53 (2024) 14171–14181, https://doi.org/10.1039/D4DT01667J.
[10] C. Carucci, L. Bruen, V. Gascón, F. Paradisi, E. Magner, Significant enhancement of structural stability of the hyperhalophilic ADH from haloferax volcanii via entrapment on metal organic framework support, Langmuir 34 (2018) 8274–8280, https://doi.org/10.1021/acs.langmuir.8b01037.
[11] M. Naseri, F. Pitzalis, C. Carucci, L. Medda, L. Fotouhi, E. Magner, A. Salis, Lipase and laccase encapsulated on zeolite imidazolate framework: enzyme activity and stability from voltammetric measurements, ChemCatChem 10 (2018) 5425–5433, https://doi.org/10.1002/cctc.201801293.
[12] G.R. Delpiano, D. Tocco, L. Medda, E. Magner, A. Salis, Adsorption of malachite green and alizarin red S dyes using Fe-BTC metal organic framework as adsorbent, Int. J. Mol. Sci. 22 (2021) 788, https://doi.org/10.3390/ijms22020788.
[13] M.I. Severino, A. Al Mohtar, C. Vieira Soares, C. Freitas, N. Sadovnik, S. Nandi, G. Mouchaham, V. Pimenta, F. Nouar, M. Daturi, G. Maurin, M.L. Pinto, C. Serre, MOFs with Open Metal(III) sites for the environmental capture of polar volatile organic compounds, Angew. Chem. Int. Ed. Engl. 62 (2023), https://doi.org/10.1002/anie.202211583.
[14] S.P. Santoso, A.E. Angkawijaya, V. Bundjaja, F.E. Soetaredjo, S. Ismadji, Metal–organic frameworks and their hybrid composites for adsorption of volatile organic compounds, in: Appl. Met. Fram. Their Deriv. Mater., Wiley, 2020, pp. 313–355, https://doi.org/10.1002/9781119651079.ch12.
[15] F. Porpora, L. Dei, C. Forcellini, C. D'Aleo, L. Lisi, M. De Sanctis, E. Carretti, Interactions between polyethyleneimine xerogels and acetic acid vapor from degraded cellulose acetate. A novel therapy for motion picture films affected by the "Vinegar Syndrome, Macromol. Rapid Commun. 46 (2025) e2500075, https://doi.org/10.1002/marc.202500075.
[16] I. Kraševec, J. Markelj, A. Elnaggar, I.K. Cigić, Indoor air pollutants and their seasonal monitoring in European museums, Herit. Sci. 12 (2024) 50, https://doi.org/10.1186/s40494-024-01164-x.
[17] K. Dedecker, R.S. Pillai, F. Nouar, J. Pires, N. Steunou, E. Dumas, G. Maurin, C. Serre, M.L. Pinto, Metal-organic frameworks for cultural heritage preservation: the case of acetic acid removal, ACS Appl. Mater. Interf. 10 (2018) 13886–13894, https://doi.org/10.1021/acsami.8b02930.
[18] A. Al Mohtar, M.I. Severino, P. Tignol, L. Ranza, A. Neves, F. Nouar, V. Pimenta, J. Lopes, A.M. Ramos, J.I.L. Rodrigo, M.J. Melo, N. Wallaszkovits, M.L. Pinto, A.-L. Dupont, C. Serre, B. Lavédrine, Iron(III) based metal-organic frameworks in cellulose acetate film preservation: fundamental aspects and first application, J. Cult. Herit. 66 (2024) 236–243, https://doi.org/10.1016/j.culher.2023.11.013.
[19] A. Dhakshinamoorthy, M. Alvaro, P. Horcajada, E. Gibson, M. Vishnuvarthan, A. Vimont, J.-M. Grenèche, C. Serre, M. Daturi, H. Garcia, Comparison of porous iron trimesates basolite F300 and MIL-100(Fe) As heterogeneous catalysts for Lewis acid and oxidation reactions: roles of structural defects and stability, ACS Catal. 2 (2012) 2060–2065, https://doi.org/10.1021/cs300345b.
[20] L. Sciortino, A. Alessi, F. Messina, G. Buscarino, F.M. Gelardi, Structure of the FeBTC metal-organic framework: a model based on the local environment study, J. Phys. Chem. C 119 (2015) 7826–7830, https://doi.org/10.1021/acs.jpcc.5b01336.
[21] A. Dhakshinamoorthy, M. Alvaro, H. Garcia, Atmospheric-pressure, liquid-phase, selective aerobic oxidation of alkanes catalysed by metal–organic frameworks, Chem. – A Eur. J. 17 (2011) 6256–6262, https://doi.org/10.1002/chem.201002664.
[22] M. Sanchez-Sanchez, I. de Asua, D. Ruano, K. Diaz, Direct synthesis, structural features, and enhanced catalytic activity of the basolite F300-like semiamorphous Fe-BTC framework, Cryst. Growth Des. 15 (2015) 4498–4506, https://doi.org/10.1021/acs.cgd.5b00755.
[23] J. Łuczak, M. Kroczewska, M. Baluk, J. Sowik, P. Mazierski, A. Zaleska-Medynska, Morphology control through the synthesis of metal-organic frameworks, Adv. Colloid Interf. Sci. 314 (2023) 102864, https://doi.org/10.1016/j.cis.2023.102864.
[24] R.S. Forgan, Modulated self-assembly of metal–organic frameworks, Chem. Sci. 11 (2020) 4546–4562, https://doi.org/10.1039/D0SC01356K.
[25] Z. Hu, I. Castano, S. Wang, Y. Wang, Y. Peng, Y. Qian, C. Chi, X. Wang, D. Zhao, Modulator effects on the water-based synthesis of Zr/Hf metal–organic frameworks: quantitative relationship studies between modulator, synthetic condition, and performance, Cryst. Growth Des. 16 (2016) 2295–2301, https://doi.org/10.1021/acs.cgd.6b00076.
[26] A.F. Sapnik, I. Bechis, A.M. Bumstead, T. Johnson, P.A. Chater, D.A. Keen, K. E. Jelfs, T.D. Bennett, Multivariate analysis of disorder in metal–organic frameworks, Nat. Commun. 13 (2022) 2173, https://doi.org/10.1038/s41467-022-29849-6.
[27] A.J. Cruz, J. Pires, A.P. Carvalho, M. Brotas de Carvalho, Adsorption of acetic acid by activated carbons, zeolites, and other adsorbent materials related with the preventive conservation of lead objects in museum showcases, J. Chem. Eng. Data 49 (2004) 725–731, https://doi.org/10.1021/je034273w.
[28] A. Zuliani, D. Chelazzi, R. Mastrangelo, R. Giorgi, P. Baglioni, Adsorption kinetics of acetic acid into ZnO/castor oil-derived polyurethanes, J. Colloid Interface Sci. 632 (2023) 74–86, https://doi.org/10.1016/j.jcis.2022.11.049.
[29] N. Chiron, R. Guilet, E. Deydier, Adsorption of Cu(II) and Pb(II) onto a grafted silica: isotherms and kinetic models, Water Res. 37 (2003) 3079–3086, https://doi.org/10.1016/S0043-1354(03)00156-8.
[30] A. Calvi, A. Ferrari, L. Sbuelz, A. Goldoni, S. Modesti, Recognizing physisorption and chemisorption in carbon nanotubes gas sensors by double exponential fitting of the response, Sensors 16 (2016) 731, https://doi.org/10.3390/s16050731.
[31] V. Gascón, C. Carucci, M.B. Jiménez, R.M. Blanco, M. Sánchez-Sánchez, E. Magner, Rapid in situ immobilization of enzymes in metal-organic framework supports under mild conditions, ChemCatChem 9 (2017) 1182–1186, https://doi.org/10.1002/cctc.201601342.

[32] Y. Yang, Y. Bai, F. Zhao, E. Yao, J. Yi, C. Xuan, S. Chen, Effects of metal organic framework Fe-BTC on the thermal decomposition of ammonium perchlorate, RSC Adv. 6 (2016) 67308–67314, https://doi.org/10.1039/C6RA12634K.
[33] H. Lv, H. Zhao, T. Cao, L. Qian, Y. Wang, G. Zhao, Efficient degradation of high concentration azo-dye wastewater by heterogeneous Fenton process with iron-based metal-organic framework, J. Mol. Catal. A Chem. 400 (2015) 81–89, https://doi.org/10.1016/j.molcata.2015.02.007.
[34] B. Pangkumhang, P. Jutaporn, K. Sorachoti, P. Khamdahsag, V. Tanboonchuy, Applicability of iron (III) trimesic (Fe-BTC) to enhance lignin separation from pulp and paper wastewater, Sains Malays. 48 (2019) 199–208. 10.17576/jsm-2019-4801-23.
[35] R. Mastrangelo, D. Chelazzi, G. Poggi, E. Fratini, L. Pensabene Buemi, M. L. Petruzzellis, P. Baglioni, Twin-chain polymer hydrogels based on poly(vinyl alcohol) as new advanced tool for the cleaning of modern and contemporary art, Proc. Natl. Acad. Sci. 117 (2020) 7011–7020, https://doi.org/10.1073/pnas.1911811117.
[36] O. Spalla, S. Lyonnard, F. Testard, Analysis of the small-angle intensity scattered by a porous and granular medium, J. Appl. Crystallogr. 36 (2003) 338–347, https://doi.org/10.1107/S0021889803002279.
[37] X. Wang, L. He, J. Sumner, S. Qian, Q. Zhang, H. O'Neill, Y. Mao, C. Chen, A.M. Al-Enizi, A. Nafady, S. Ma, Spatially confined protein assembly in hierarchical mesoporous metal-organic framework, Nat. Commun. 14 (2023) 973, https://doi.org/10.1038/s41467-023-36533-w.
[38] X. Xing, W. Cheng, S. Zhou, H. Liu, Z. Wu, Recent advances in small-angle scattering techniques for MOF colloidal materials, Adv. Colloid Interf. Sci. 329 (2024) 103162, https://doi.org/10.1016/j.cis.2024.103162.
[39] E.A. Chavez Panduro, T. Beuvier, M. Fernández Martínez, L. Hassani, B. Calvignac, F. Boury, A. Gibaud, Small-angle X-ray scattering analysis of porous powders of CaCO 3, J. Appl. Crystallogr. 45 (2012) 881–889, https://doi.org/10.1107/S0021889812032219.
[40] W. Wong-Ng, J.A. Kaduk, D.L. Siderius, A.L. Allen, L. Espinal, B.M. Boyerinas, I. Levin, M.R. Suchomel, J. Ilavsky, L. Li, I. Williamson, E. Cockayne, H. Wu, Reference diffraction patterns, microstructure, and pore-size distribution for the copper (II) benzene-1,3,5-tricarboxylate metal organic framework (Cu-BTC) compounds, Powder Diffr. 30 (2015) 2–13, https://doi.org/10.1017/S0885715614001195.
[41] A. Laurikėnas, J. Barkauskas, J. Reklaitis, G. Niaura, D. Baltrūnas, A. Kareiva, Formation peculiarities of iron (III) acetate: potential precursor for iron metal-organic frameworks (MOFs), Lith. J. Phys. 56 (2016) 35–41, https://doi.org/10.3952/PHYSICS.V56I1.3274.
[42] J.-K. Kim, H.-S. Oh, C.-W. Jo, Y.-J. Suh, H.-D. Jang, K.-K. Koo, Recovery of iron as a form of ferrous acetate precipitates from low-grade magnetite ore, Chem. Eng. Res. Des. 88 (2010) 1467–1473, https://doi.org/10.1016/j.cherd.2009.08.011.
[43] K. Sakata, S. Kashiyama, G. Matsuo, S. Uemura, N. Kimizuka, M. Kunitake, Growth of two-dimensional metal–organic framework nanosheet crystals on graphite substrates by thermal equilibrium treatment in acetic acid vapor, ChemNanoMat 1 (2015) 259–263, https://doi.org/10.1002/cnma.201500062.
[44] T. Tsuruoka, S. Furukawa, Y. Takashima, K. Yoshida, S. Isoda, S. Kitagawa, Nanoporous nanorods fabricated by coordination modulation and oriented attachment growth, Angew. Chemie Int. Ed. 48 (2009) 4739–4743, https://doi.org/10.1002/anie.200901177.
[45] C. Pathak, S. Mistry, S. Seth, Morphological variation of metal-organic frameworks and its impacts on their functional properties, Coord. Chem. Rev. 543 (2025) 216928, https://doi.org/10.1016/j.ccr.2025.216928.